



Cite this: *Phys. Chem. Chem. Phys.*,
2018, 20, 7317

CO oxidative coupling to dimethyl oxalate over Pd–Me (Me = Cu, Al) catalysts: a combined DFT and kinetic study

Bingying Han,^a Xue Feng,^b Lixia Ling,^{*bcd} Maohong Fan,^{id c} Ping Liu,^d
Riguang Zhang^a and Baojun Wang^{id *a}

CO oxidative coupling to dimethyl oxalate (DMO) on Pd(111), Pd–Cu(111) and Pd–Al(111) surfaces was systematically investigated by means of density functional theory (DFT) together with periodic slab models and micro-kinetic modeling. The binding energy results show that Cu and Al can be fine substrates to stably support Pd. The favorable pathway for DMO synthesis on these catalysts starts from the formation of two COOCH₃ intermediates, followed by the coupling to each other, and the catalytic activity follows the trend of Pd–Al(111) > Pd(111) > Pd–Cu(111). Additionally, the formation of DMO is far favorable than that of dimethyl carbonate (DMC) on these catalysts. The results were further demonstrated by micro-kinetic modeling. Therefore, Pd–Al bimetallic catalysts can be applied in practice to effectively enhance the catalytic performance and greatly reduce the cost. This study can help with fine-tuning and designing of high-efficient and low-cost Pd-based bimetallic catalysts.

Received 12th December 2017,
Accepted 7th February 2018

DOI: 10.1039/c7cp08306h

rsc.li/pccp

1. Introduction

Coal to ethylene glycol (CTEG)^{1–5} as a new EG synthesis technology has attracted substantial attention because of its green and atomic economy, which can greatly enhance the efficient and clean utilization of coal resources. CO oxidative coupling to dimethyl oxalate (DMO) is the crucial step in the realization of the conversion of inorganic C1 to organic C2 in CTEG,⁶ and it is considered to be one of the most important applications in C1 chemistry. This process includes two major chemical reactions: (1) DMO synthesis: $2\text{CO} + 2\text{CH}_3\text{ONO} \rightarrow (\text{COOCH}_3)_2 + 2\text{NO}$; and (2) CH₃ONO regeneration: $2\text{NO} + 2\text{CH}_3\text{OH} + 1/2\text{O}_2 \rightarrow 2\text{CH}_3\text{ONO} + \text{H}_2\text{O}$. Among these, CH₃ONO can easily dissociate into NO and OCH₃ on palladium-based catalysts,^{7,8} the generated NO can desorb directly⁹ and react quickly with methanol and oxygen to form CH₃ONO without any catalyst,¹⁰ and the generated OCH₃ initiates the reaction of CO oxidative coupling to form DMO on

palladium-based catalysts.⁷ The overall chemical process is an environmentally friendly technology with mild reaction conditions and low energy consumption. In addition, lots of CO exhausts from steelmaking plants, coke oven, vehicles, *etc.*, cause serious environmental pollution and resource waste. Therefore, CO oxidative coupling to DMO can not only sufficiently utilize the CO exhausts to produce valuable chemicals, but also effectively reduce environmental pollution.

Palladium-based catalysts have been proved to be promising and effective catalysts for CO oxidative coupling to DMO,^{7,11–18} which exhibited high activity, selectivity and stability, and the exposed (111) facet was identified as the active plane in catalysis.¹¹ However, Pd metal is too expensive for the commercial application, and the Pd loading of industrial catalysts for CO oxidation to DMO is still relatively high at 2 wt% (the state of the art), resulting in a great increase in the cost of production. Moreover, the shortage of noble metal resources is more and more serious in the world along with their large consumption in various industrial catalysts and the jewellery industry. Thus, how to reduce the amount of Pd catalyst and keep or improve its catalytic performance for this process is an urgent problem.

Bimetallic catalysts^{19–27} have attracted tremendous attention due to their electronic and chemical properties distinct from those of monometallic ones, which provide the opportunities to develop novel catalysts with increased activity, selectivity, and stability through lattice strain,²⁵ ligand,²⁰ geometric,^{19,20,24} electronic,^{19,24} or bifunctional²³ effects. Additionally, bimetallic

^a Key Laboratory of Coal Science and Technology of Ministry of Education and Shanxi Province, Taiyuan University of Technology, No. 79 West Yingze Street, Taiyuan 030024, P. R. China. E-mail: wangbaojun@tyut.edu.cn; Fax: +86 351 6041237; Tel: +86 351 6010898

^b College of Chemistry and Chemical Engineering, Taiyuan University of Technology, No. 79 West Yingze Street, Taiyuan 030024, P. R. China. E-mail: linglixia@tyut.edu.cn

^c Department of Chemical and Petroleum Engineering, University of Wyoming, 1000 E University Ave, Laramie, WY 82071, USA

^d State Key Laboratory of Coal Conversion, Institute of Coal Chemistry, Chinese Academy of Sciences, Taiyuan 030001, P. R. China

catalysts can also show promise of replacing noble metal catalysts with enhanced catalytic performance, but low-cost catalysts which are composed of noble and cheap metals.^{28–33} As for bimetallic catalyst synthesis, a variety of solution-based synthetic methods have been established, which include co-reduction, thermal decomposition, seeded-growth, galvanic replacement reaction, and the noble-metal-induced-reduction (NMR) strategy.²²

More recently, it has been reported that Pd-based bimetallic catalysts have been widely studied experimentally and theoretically, such as Pd–Fe,^{34,35} Pd–Mg,³⁶ Pd–Ag,³⁷ Pd–Ni,³⁸ and Pd–Co,³⁹ where the noble metal Pd generally occupies surface layers with cheap metals as substrates, in order to increase their catalytic activities by the synergistic effect and reduce the cost of the catalysts. In addition, Cu and Al, which are much cheaper than Pd, have also been widely considered to be substrates to synthesize Pd-based bimetallic catalysts. For example, Kyriakou *et al.*⁴⁰ studied the selective hydrogenation of styrene and acetylene on Pd atoms deposited on the Cu(111) surface and found it exhibited high activity compared with pure Cu or Pd metal alone. Additionally, Cu@Pd/C core-shell bimetallic catalysts were synthesized using an aqueous method and showed excellent activity and stability toward formic acid oxidation (FAO) than Pd/C.⁴¹ The experimental results were further demonstrated using DFT calculations, where Cu@Pd bimetallic catalysts were modeled by Pd monolayers placed on the top of the Cu(111) surface, indicating that the Pd–Cu(111) surface could well reflect the catalytic performance of Cu@Pd bimetallic catalysts toward FAO. And, Pd-based bimetallic catalysts with Cu, Al, Mn, Zn, Fe, Sn, and Mg were synthesized by depositing Pd onto these metal substrates, to explore the influence of metal substrates on hydrodechlorination reactivity of 2-chlorobiphenyl.⁴² Among these catalysts, Pd–Al bimetallic catalysts presented the highest stability and relatively high reactivity. Al was also proved to be a fine metal substrate to support tiny Pd, which exhibited a high catalytic performance to biodegradable phenol.⁴³ Additionally, the strong interaction between monolayer Pd and Al substrates was attributed to the hybridization of the Pd d orbital and Al p orbital.^{44–48} The adsorption of halogen (Cl, Br and I) was studied on Pd–M(111) surfaces, where the palladium monolayer was deposited on M(111) surfaces (Me = Cu, Au or Pt).⁴⁹ It was found that the adsorption energies of halogen atoms depended roughly linearly on the d-band centers of substrates. Additionally, a novel core-shell Al₁₃@Pt₄₂ bimetallic catalyst was developed to increase Pt utilization for the oxygen reduction reaction in fuel cells using DFT calculations.⁵⁰ The results showed that the Al₁₃@Pt₄₂ cluster possessed high catalytic activity, and the Pt atoms at the edge sites were effectively activated by Pt–Al bonds, greatly increasing its utilization efficiency. Moreover, it also exhibited excellent cluster stability because of the strong orbital hybridization of the p band of the Al₁₃ core and the d band of the Pt₄₂ shell, which indicated that the Al₁₃ core can exist stably without being oxidized in catalysis. These types of DFT calculations, coupled with parallel experimental efforts, will offer fruitful opportunities for the rational design of bimetallic catalysts that are low in cost and that exhibit a high catalytic performance.

As mentioned above, Pd–Cu or Pd–Al bimetallic catalysts exhibited excellent catalytic activity and stability for chemical reactions,^{41–43} however, there are few systematic and comparative

studies about DMO synthesis on Pd–Cu and Pd–Al bimetallic catalysts. Besides, the microscopic mechanism about controlling the catalytic performance of the catalysts is still unclear. Therefore, in this work, we carried out a systematic study using DFT together with periodic slab models and micro-kinetic modeling to investigate CO oxidative coupling to DMO over Pd(111), Pd–Cu(111) and Pd–Al(111) surfaces. It is expected that the study can provide a good clue for designing a high-efficient and low-cost Pd-based bimetallic catalysts for DMO synthesis.

2. Methodology and models

All the calculations were performed using the Vienna ab initio simulation package (VASP),^{51,52} in which the electron–ion interactions were expressed using the projector-augmented wave (PAW) method.^{53,54} The generalized gradient approximation (GGA) with Perdew–Burke–Ernzerhof (PBE)⁵⁵ was used to describe the exchange–correlation energies and potential. A plane wave basis set with a cutoff energy of 400 eV and a (3 × 2 × 1) *k*-point grid generated with the Monkhorst–Pack scheme were found to give converged results. The atomic structures were relaxed using the conjugate gradient algorithm as implemented in the VASP code until the electronic energy and forces on all unconstrained atoms became less than 1 × 10^{−5} eV and 0.03 eV Å^{−1}, respectively. Transition states were located by combining the climbing-image nudged elastic band method (CI-NEB)^{56,57} and the dimer method,^{58,59} where a linear interpolation between reactant and product states was used to find saddle points between the known reactants and products for all NEB calculations, and the initial guess for the transition state structure was optimized using the dimer method. In this study, the forces for all atoms of the optimized transition state structure using the dimer method were less than 0.05 eV Å^{−1}. The transition states were further confirmed using vibrational frequency calculations, in which only one imaginary frequency was obtained at the saddle point.

The lattice constants calculated for bulk Pd, Cu and Al are 3.955, 3.623 and 3.992 Å, respectively, which are in good agreement with the experimental values (Pd, 3.891; Cu, 3.615; Al, 4.049 Å).⁶⁰ The pure Pd(111), Cu(111) and Al(111) surfaces are modeled using a three-layer supercell with dimensions of 3 × 4 × 1. In light of previous work,⁴⁹ Pd–Cu(111) and Pd–Al(111) surfaces are constructed by substituting the top layer atoms of pure Cu(111) and Al(111) surfaces with Pd atoms, which are employed to represent the Pd monolayer supported on Cu and Al substrates. The corresponding Pd–Pd bond lengths calculated are 2.650 and 2.863 Å, respectively, (that of pure Pd(111) is 2.797 Å), indicating that the bond length of palladium is decreased by Cu but improved by Al. The vacuum region was set at 10 Å to separate the slabs in the direction perpendicular to the surface. During geometry optimization, the third layer is frozen in their bulk positions, and the top two layers and species are allowed to relax. The isolated molecules and radicals are optimized in a large cell of 10 × 10 × 10 Å. The side and top views of Pd(111), Pd–Cu(111) and Pd–Al(111) surfaces are shown in Fig. 1.

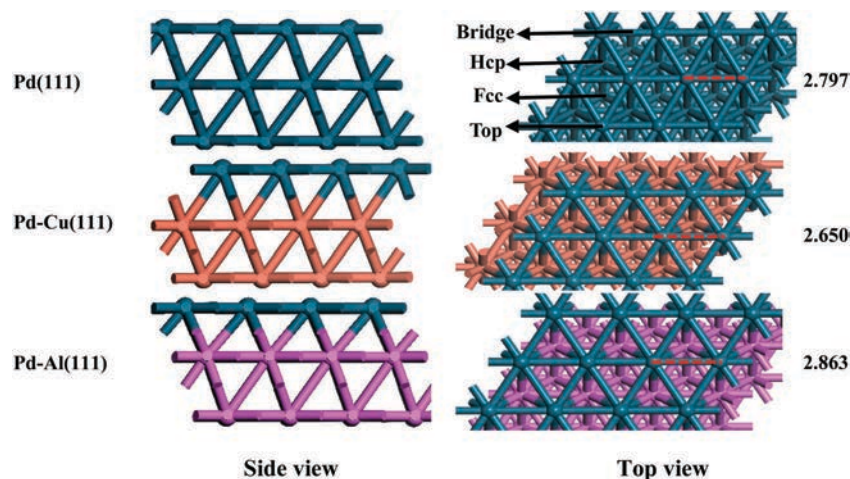


Fig. 1 Side and top views of the optimized configurations of Pd(111), Pd-Cu(111) and Pd-Al(111) surfaces and the corresponding adsorption sites. Dark cyan, orange, and violet red balls denote Pd, Cu and Al atoms, respectively. (Bond length: Å.)

The adsorption energy, E_{ads} , is defined using the following eqn (1) and (2):

$$E_{\text{ads}} = (E_{\text{slab/adsorbate}} - E_{\text{slab}} - E_{\text{adsorbate}}) + \Delta\text{ZPE}_{\text{ads}} \quad (1)$$

$$\Delta\text{ZPE}_{\text{ads}} = \left(\sum_{i=1}^{\text{Vibrations}} \frac{hf_i}{2} \right)_{\text{slab/adsorbate}} - \left(\sum_{i=1}^{\text{Vibrations}} \frac{hf_i}{2} \right)_{\text{adsorbate}} \quad (2)$$

where $E_{\text{slab/adsorbate}}$ is the total energy of the slab and adsorbate system; E_{slab} is the energy of Pd(111), Pd-Cu(111) and Pd-Al(111) surfaces; $E_{\text{adsorbate}}$ is the energy of the isolated adsorbate; $\Delta\text{ZPE}_{\text{ads}}$ refers to the zero-point vibrational energy, which is used to calculate the ZPE correction *via* the vibrational frequencies (f_i) for the species only including the gas phase and the adsorbed state. This is because that compared with their large vibrational contribution, the contribution of solid surfaces is negligible for the large mass differences.⁶¹ Additionally, h is Planck's constant.

For a reaction such as R (reactant) \rightarrow P (product) on these catalyst surfaces, the activation barrier with the zero-point correction (E_a) is calculated according to eqn (3) and (4):

$$E_a = (E_{\text{TS}} - E_{\text{R}}) + \Delta\text{ZPE}_{\text{barrier}} \quad (3)$$

where E_{R} and E_{TS} are the total energies of the reactant and the transition state, respectively, and $\Delta\text{ZPE}_{\text{barrier}}$ refers to the ZPE correction for the reaction barrier.

$$\Delta\text{ZPE}_{\text{barrier}} = \left(\sum_{i=1}^{\text{Vibrations}} \frac{hf_i}{2} \right)_{\text{TS}} - \left(\sum_{i=1}^{\text{Vibrations}} \frac{hf_i}{2} \right)_{\text{R}} \quad (4)$$

The first term includes the vibrational frequencies of the species in the TS, in which the imaginary frequency has not been considered, and the second term includes the vibrational frequencies of the adsorbed reactants.

The reaction energy with the zero-point correction (ΔH) is calculated on the basis of the following formulas (5) and (6):

$$\Delta H = (E_{\text{P}} - E_{\text{R}}) + \Delta\text{ZPE}_{\text{energy}} \quad (5)$$

$$\Delta\text{ZPE}_{\text{energy}} = \left(\sum_{i=1}^{\text{Vibrations}} \frac{hf_i}{2} \right)_{\text{P}} - \left(\sum_{i=1}^{\text{Vibrations}} \frac{hf_i}{2} \right)_{\text{R}} \quad (6)$$

where $\Delta\text{ZPE}_{\text{energy}}$ refers to the ZPE correction for the reaction energy, which is determined by the vibrational frequencies of the reactants and products.

The binding energy (E_b) per Pd atom is considered for the interaction between the Pd monolayers and the bottom Pd(111), Cu(111) and Al(111) surfaces. E_b is calculated according to eqn (7):

$$E_b = (E_{\text{slab}} - E_{\text{Pd monolayer}} - E_{\text{substrate}})/n \quad (7)$$

where E_{slab} , $E_{\text{Pd monolayer}}$ and $E_{\text{substrate}}$ are the total energy, surface layer energy and bottom two layer energy of Pd(111), Pd-Cu(111) and Pd-Al(111) surfaces, respectively ($n = 12$, the number of surface Pd atoms).

The d-band center is calculated using eqn (8):^{62,63}

$$\epsilon_d = \frac{\int_{-\infty}^{+\infty} E \rho_d(E) dE}{\int_{-\infty}^{+\infty} \rho_d(E) dE} \quad (8)$$

where ρ_d represents the density of states projected onto the d-band of the surface Pd monolayer of Pd(111), Pd-Cu(111) and Pd-Al(111) surfaces and E is the energy of the d-band.

In this work, the binding energy, d-band center and the adsorption energy of CO on Pd(111), Pd-Cu(111) and Pd-Al(111) surfaces with three, four and five-layer are calculated to confirm the sufficiency of the selected three-layer models. The results indicate that the binding energies are -1.19 , -1.20 and -1.22 eV per atom on Pd(111) surfaces with three, four and five-layer, respectively. Similarly, they are -1.32 , -1.27 and -1.30 eV per atom on Pd-Cu(111) surfaces, respectively. On the different Pd-Al(111) surfaces, the binding energies are -2.03 , -2.08 and -2.06 eV per atom. It implies that there exists little difference in the same catalysts with different layers. Further, d-band centers of Pd monolayers on Pd(111), Pd-Cu(111) and Pd-Al(111) surfaces with three-layer are compared with that on four and five-layer models. They are -1.87 , -1.89 and -1.90 eV on Pd(111) surfaces,

−2.18, −2.23 and −2.14 eV on Pd–Cu(111) surfaces, −2.79, −2.80 and −2.83 eV on Pd–Al(111) surfaces. It can be seen that they are close to each other on the same catalysts with different layers. In addition, adsorption energies of CO at the top site on catalysts with four and five-layer models (the top two layers with adsorbates are relaxed, and the other bottom layers are fixed to their bulk positions) are calculated. The corresponding adsorption energies of CO are −129.9 and −126.7 kJ mol^{−1} on the Pd(111) surface, −79.0 and −76.8 kJ mol^{−1} on the Pd–Cu(111) surface, −75.5 and −73.4 kJ mol^{−1} on the Pd–Al(111) surface, which are in good agreement with the values of −132.0, −79.7 and −78.9 kJ mol^{−1} on Pd(111), Pd–Cu(111) and Pd–Al(111) surfaces using three-layer models, respectively. Therefore, considering the efficiency of calculation, three-layer models are thought to be suitable and enough for our calculated systems.

Additionally, the stability of the constructed models is very important to the following study. In light of previous work,⁵⁰ the stronger binding energy makes the higher dissolution resistance. Therefore, the binding energy is employed to evaluate the stability of Pd monolayers on Pd(111), Cu(111) and Al(111) surfaces. As mentioned above, the binding energies are −1.19, −1.32 and −2.03 eV per atom on Pd(111), Pd–Cu(111) and Pd–Al(111) surfaces, which indicate that these structures are thermodynamic stable, and Cu and Al can be fine substrates to support Pd monolayers. In order to exactly elucidate the interaction between the surface Pd atoms and substrates, the Bader charge analysis is executed. The results show that the average electron transfers from substrates to surface Pd monolayers are 0.03, 0.14 and 1.74 *e* on Pd(111), Pd–Cu(111) and Pd–Al(111) surfaces, respectively. It is clear that the addition of Cu and Al has effects on the electronic properties rather than the geometry of ensembles, as well as the more transfer electrons and the greater binding energy. The d-band center was also thought to have a direct influence on binding energy.^{64–66} Thence, we analyze the d-band structure of surface Pd monolayers of Pd(111), Pd–Cu(111) and Pd–Al(111) surfaces, as shown in Fig. 2.

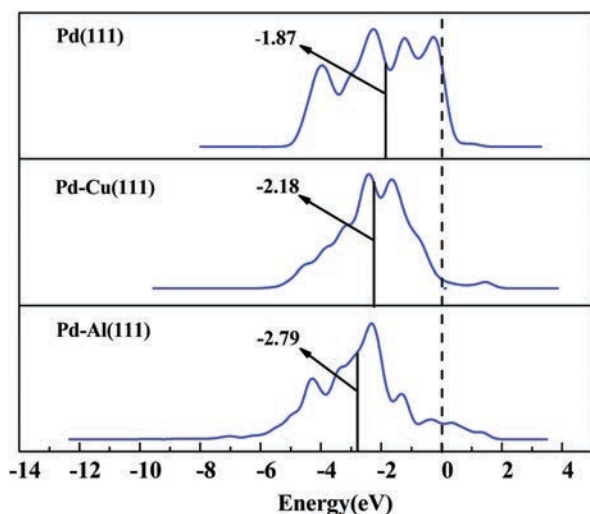


Fig. 2 The PDOS of surface Pd monolayers on Pd(111), Pd–Cu(111) and Pd–Al(111) surfaces (the vertical solid line represents the location of the d-band centers, the vertical dotted line represents the location of the Fermi level.)

The d-band centers of surface Pd monolayers are −1.87, −2.18 and −2.79 eV, respectively, suggesting that the d-band center is farther away from the Fermi level, shifting to the low energy region and the Pd monolayer is more stable.

3. Results and discussion

3.1 Adsorption of reactants, possible intermediates and products

In this section, various possible adsorption configurations (top, bridge, hcp and fcc) of reactants, intermediates, and products are investigated in CO oxidative coupling to DMO over Pd(111), Pd–Cu(111) and Pd–Al(111) surfaces. The corresponding adsorption energies with the zero-point vibrational energy (ZPE) correction are listed in Table 1 and the configurations are shown in Fig. 3, as well as the detailed description is discussed as follows.

CO binds to these catalyst surfaces through C atoms at top, bridge, hcp and fcc sites, except that CO cannot stably exist on the bridge site on the Pd–Al(111) surface. On the Pd(111) surface, the corresponding adsorption energies are −132.0, −170.1, −187.4 and −188.1 kJ mol^{−1}, respectively, which are in good agreement with the reference values (130.8, 174.0, 190.4 and 193.3 kJ mol^{−1}, respectively).⁶⁷ The adsorption energies of CO are −79.7, −124.7, −149.2 and −145.6 kJ mol^{−1} at four sites on the Pd–Cu(111) surface, and they are −78.9, −84.6, and −84.8 kJ mol^{−1} at top, hcp and fcc sites on the Pd–Al(111) surface, respectively. The results show that the adsorption energies of CO at hcp and fcc sites on the same catalyst are very close, and Pd–Cu and Pd–Al bimetallic catalysts can decrease the adsorption strength of CO.

OCH₃ is adsorbed *via* O atoms on the Pd(111) surface at top, bridge, hcp and fcc sites, the corresponding adsorption energies are −143.8, −157.0, −155.0 and −170.1 kJ mol^{−1}. Similarly, OCH₃ also

Table 1 The adsorption energies with the zero-point vibrational energy (ZPE) correction of all possible species involving in CO oxidative coupling to DMO on Pd(111), Pd–Cu(111) and Pd–Al(111) surfaces

		E_{ads} (kJ mol ^{−1})			
		Top	Bridge	Hcp	Fcc
Pd(111)	CO	−132.0	−170.1	−187.4	−188.1
	OCH ₃	−143.8	−157.0	−155.0	−170.1
	COOCH ₃	−198.9	−209.9	—	—
	OCCOOCH ₃	−187.9	−228.7	—	—
	DMO	−13.6	—	—	—
	DMC	−13.0	—	—	—
Pd–Cu(111)	CO	−79.7	−124.7	−149.2	−145.6
	OCH ₃	−102.6	−100.4	−94.0	−101.4
	COOCH ₃	−162.6	−155.7	—	—
	OCCOOCH ₃	−155.5	−149.2	—	—
	DMO	−14.9	—	—	—
	DMC	−14.4	—	—	—
Pd–Al(111)	CO	−78.9	—	−84.6	−84.8
	OCH ₃	−137.5	−153.8	−162.1	−159.8
	COOCH ₃	−155.0	—	—	—
	OCCOOCH ₃	−132.8	—	—	—
	DMO	−11.3	—	—	—
	DMC	−12.1	—	—	—

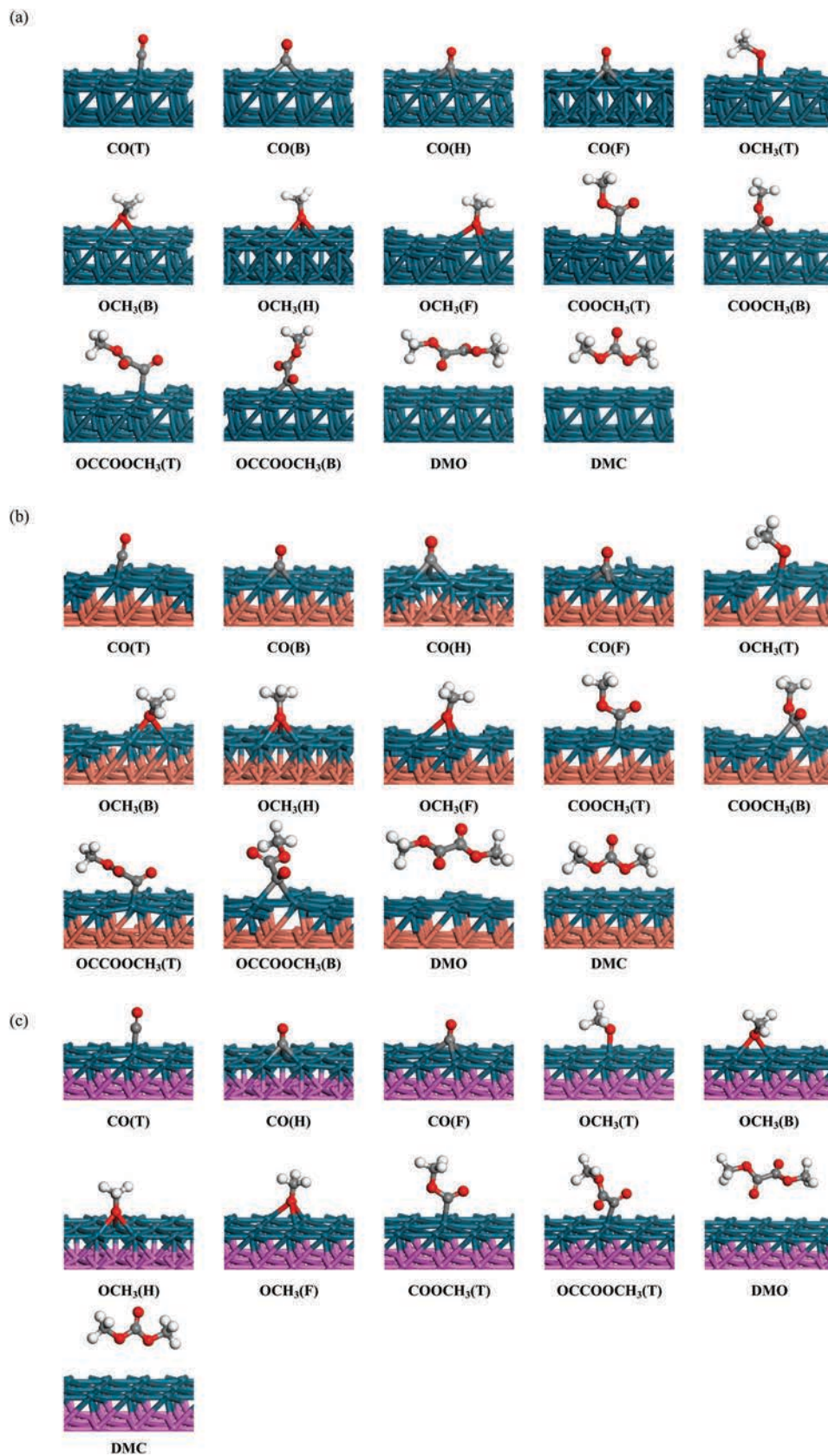


Fig. 3 Adsorption configurations of all possible species involving in CO oxidative coupling to DMO on (a) Pd(111), (b) Pd-Cu(111) and (c) Pd-Al(111) surfaces. Dark cyan, orange, violet red, grey, white and red balls denote Pd, Cu, Al, C, H, and O atoms, respectively. The same color scheme is applied in Fig. 5–8.

connects with the four sites on Pd-Cu(111) and Pd-Al(111) surfaces, the corresponding adsorption energies on the Pd-Cu(111) surface are -102.6 , -100.4 , -94.0 and -101.4 kJ mol^{-1} , as well as those on the Pd-Al(111) surface are -137.5 , -153.8 , -162.1 and -159.8 kJ mol^{-1} , respectively. The results show that the adsorption energies of OCH_3 at bridge and hcp sites on the Pd(111) surface are very close. The same results have also been obtained at top, bridge, and fcc sites on the Pd-Cu(111) surface, and at bridge, hcp and fcc sites on the Pd-Al(111) surface. The adsorption strength of OCH_3 on Pd-Cu(111) and Pd-Al(111) surfaces is also decreased, except that of OCH_3 at the hcp site on the Pd-Al(111) surface.

COOCH_3 and OCCOOCH_3 only occupy the top and bridge sites on Pd(111) and Pd-Cu(111) surfaces *via* C atoms, because they are not stable at hcp and fcc sites, which easily migrate to the bridge site. The adsorption energies of COOCH_3 are -198.9 and -209.9 kJ mol^{-1} at top and bridge sites on the Pd(111) surface, and they are -162.6 and -155.7 kJ mol^{-1} on the Pd-Cu(111) surface, respectively. The adsorption energies of OCCOOCH_3 are -187.9 and -228.7 kJ mol^{-1} at top and bridge sites on the Pd(111) surface, and they are -155.5 and -149.2 kJ mol^{-1} on the Pd-Cu(111) surface. Additionally, COOCH_3 and OCCOOCH_3 only occupy the top site on the Pd-Al(111) surface through C atoms, and the corresponding adsorption energies are -155.0 and -132.8 kJ mol^{-1} , respectively. The adsorption energies of COOCH_3 and OCCOOCH_3 were also decreased on Pd-Cu(111) and Pd-Al(111) surfaces.

DMO and DMC are weakly adsorbed upon these catalysts due to typical physisorption. The adsorption energies of DMO are -13.6 , -14.9 and -11.3 kJ mol^{-1} on Pd(111), Pd-Cu(111) and Pd-Al(111) surfaces, as well as the adsorption energies of DMC are -13.0 , -14.4 and -12.1 kJ mol^{-1} , respectively.

From the above we can see that the addition of Cu or Al to palladium catalysts can reduce the adsorption strength of CO, OCH_3 , COOCH_3 and OCCOOCH_3 species except that of OCH_3 at the hcp site on the Pd-Al(111) surface.

3.2 Reaction pathways for CO oxidative coupling to DMO on Pd(111), Pd-Cu(111) and Pd-Al(111) surfaces

On the basis of the adsorption results, CO oxidative coupling to DMO on Pd(111), Pd-Cu(111) and Pd-Al(111) surfaces was studied. Since CH_3ONO can easily dissociate into the OCH_3 and NO on Pd-based catalysts,^{7,8} the dissociation of CH_3ONO will not be discussed in the following sections and the OCH_3

radical initiates the reaction of CO oxidative coupling to form DMO. According to previous work,⁷ three possible pathways for CO oxidation to DMO have been considered, namely the COOCH_3 - COOCH_3 coupling route (Path1), the CO - COOCH_3 coupling route (Path2) and the CO - CO coupling route (Path3), as shown in Fig. 4. Additionally, due to the co-existence of OCH_3 and COOCH_3 , the pathway for CO oxidation to dimethyl carbonate ($\text{CH}_3\text{OCOCH}_3$, DMC) was also considered. However, only two pathways (Path1 and Path2) are obtained on Pd-Cu(111) and Pd-Al(111) surfaces, since the OCCO intermediate does not stably exist.

In this work, the catalytic activity of pure Cu(111) and Al(111) surfaces for CO oxidative coupling to DMO is firstly investigated. Taking into account the calculation efficiency, the initial and final steps of DMO formation, namely, CO interacting with OCH_3 to COOCH_3 , two CO coupling to OCCO, two COOCH_3 coupling and OCCOOCH_3 interacting with OCH_3 to DMO on Cu(111) and Al(111) surfaces are studied. Either the initial or the final step cannot be occurred on Cu(111) and Al(111) surfaces, indicating that CO oxidative coupling to DMO cannot be proceeded. The results show that the CO - CO coupling path does not occur, since the OCCO intermediate does not exist on two pure surfaces. Moreover, CO interacting with OCH_3 needs an energy barrier of 49.3 kJ mol^{-1} on the Cu(111) surface, but the structure of the transition state is not obtained on the Al(111) surface. In addition, transition states are also not obtained for two COOCH_3 coupling and OCCOOCH_3 interacting with OCH_3 to DMO on the Cu(111) surface. When the structure corresponding to the change from the reactant to product is searched, it is deformed and far away from the minimum energy path. Therefore, DMO formation *via* CO oxidative coupling cannot be carried out on pure Cu(111) and Al(111) surfaces. Previous work⁶⁸ has also indicated that the transition state for CHCHO hydrogenation to CHCH_2O cannot be obtained, implying that the reaction of CHCHO to CHCH_2O does not take place on the Co(0001) surface.

Previous DFT calculation⁷ and experiment results¹¹ showed that the linear absorption mode of CO was mainly involved in CO oxidative coupling to DMO, because the weak chemical adsorption implied that species could easily move on the surface. In this work, we test the activation energies of the elementary reactions between CO at the top site and OCH_3 at four sites, as well as OCH_3 at the top site and CO at four sites on the Pd(111) surface, which are shown in Fig. 5. The results indicate that the activation

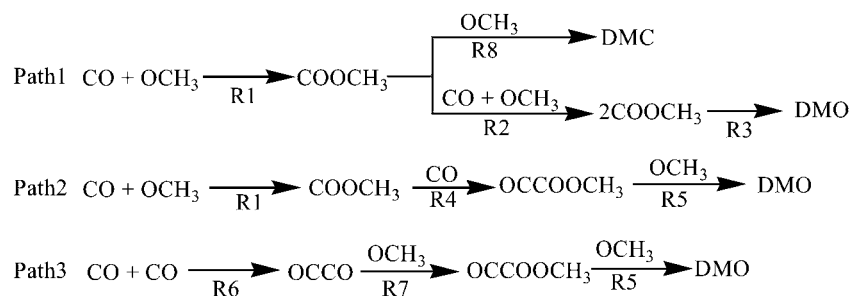


Fig. 4 Pathways of CO oxidative coupling to DMO.⁷

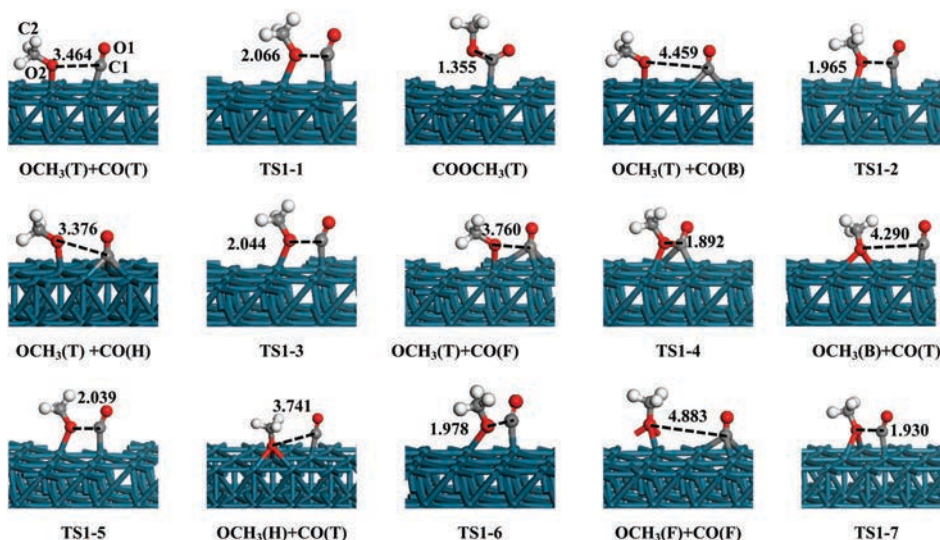
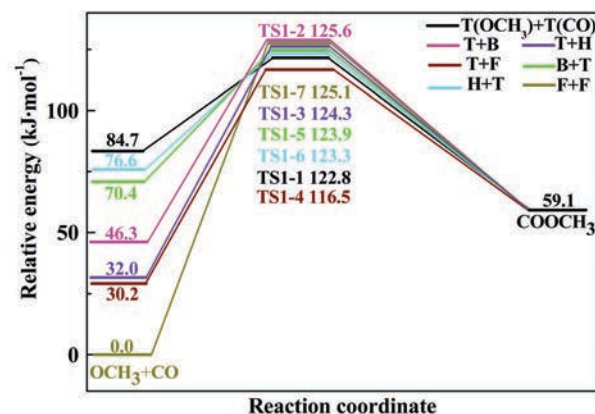


Fig. 5 Potential energy diagram of the tested elementary reactions between CO and OCH₃ and the configuration of initial states, transition states and final states on the Pd(111) surface.

energy of the reaction $\Delta E_{\text{TS1-1}} = 30.2 \text{ kJ mol}^{-1}$ which is owing to their weaker adsorption energies and shorter distance between them. Hence, the site of the species which have the above two points is preferred as the active site.

3.2.1 Reaction pathways for CO oxidative coupling to DMO on the Pd(111) surface. As shown in Fig. 5, Path1 firstly starts from the co-adsorption from CO and OCH₃ to form a stable intermediate (IS1) on the Pd(111) surface, where the adsorbed OCH₃ obliquely binds to a top site and meanwhile CO occupies the adjacent top site. Then, the adsorbed OCH₃ approaches the carbon of nearby adsorbed CO through its oxygen to form COOCH₃ sitting on the top site through C atoms with a C1–O2 bond length of 1.355 Å via a transition state TS1, where the distance between the O atom of OCH₃ and the C atom of CO decreases to 2.066 from 3.464 Å in IS1. An exothermic energy of 25.6 kJ mol⁻¹ and an energy barrier of 38.1 kJ mol⁻¹ are needed in this step.

The other COOCH₃ formation is via a transition state TS2, as shown in Fig. 6, which is exothermic (17.5 kJ mol⁻¹) with an energy barrier of 52.5 kJ mol⁻¹, finally leading to the formation of two COOCH₃ (intermediate state, IS3). In TS2, the distance of

C3 and O4 is reduced from 3.184 to 2.077 Å. Subsequently, DMO is formed by two COOCH₃ coupling to each other on the Pd(111) surface via a transition state (TS3), accompanied by a high energy barrier of 120.6 kJ mol⁻¹ and endothermic of 53.6 kJ mol⁻¹. In TS3, the distance between C1 and C3 atoms of two COOCH₃ shortens to 1.990 from 3.346 Å in IS3. In summary, R3 is the rate-determining step with a high energy barrier of 120.6 kJ mol⁻¹ in Path1, which is lower than the previous DFT calculation results (155.4 kJ mol⁻¹),⁷ it is because that the co-adsorption configuration of two COOCH₃ has a relatively weaker steric hindrance effects compared with that in the literature.

Path2 also begins with the co-adsorption of CO and OCH₃ on the Pd(111) surface. The first reaction step is the same as that of Path1. In the second step, the other CO cannot be stable in the adjacent top site due to the repulsion of COOCH₃, and migrates to the bridge site, then COOCH₃ attacks CO to form OCCOOCH₃ with a C1–C3 bond length of 1.542 Å via a transition state (TS4), accompanied by endothermic heat of 117.0 kJ mol⁻¹ with an energy barrier by 160.1 kJ mol⁻¹. In TS4, the C1–C3 distance decreases to 1.867 from 4.381 Å. In the last step, OCH₃ approaches the carbon of OCCOOCH₃ to form DMO via a transition state (TS5),

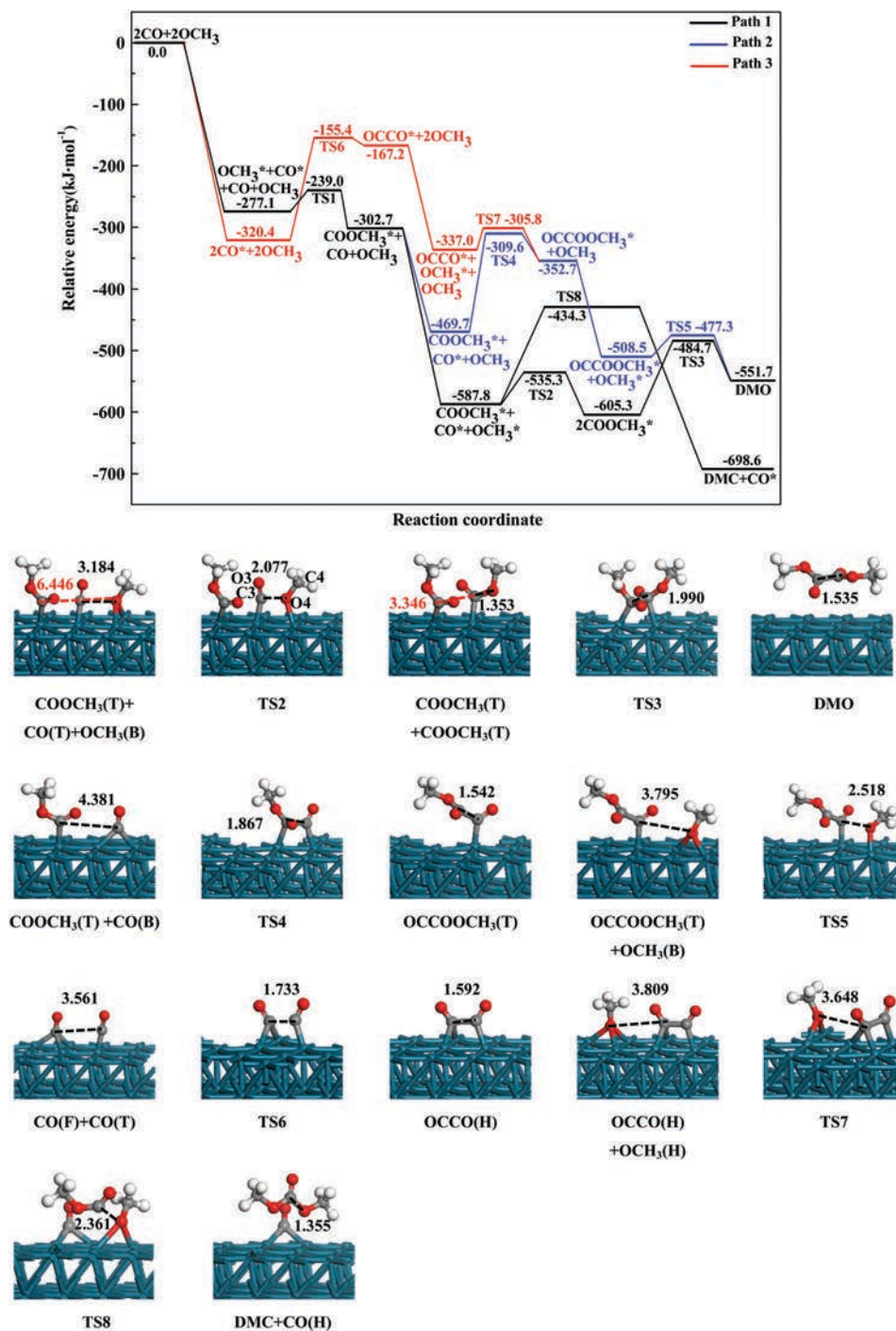


Fig. 6 Potential energy diagram of CO oxidative coupling to DMO and the corresponding configuration of initial states, transition states and final states on the Pd(111) surface.

where the distance between C3 and O4 atoms shortens from 3.795 to 2.518 Å. An energy barrier of 31.2 kJ mol⁻¹ and an exothermic heat of 43.2 kJ mol⁻¹ are needed in this process. Overall, the rate-determining step is R4 with an energy barrier of 160.1 kJ mol⁻¹ in Path2, which is higher (39.5 kJ mol⁻¹) than that in Path1.

In Path3, two CO molecules are firstly adsorbed on the Pd(111) surface, where one CO binds onto the top site and the other CO occupies the fcc site, then two CO molecules

couple to each other to form an OCCO intermediate, finally the two OCH₃ adsorbed approach the two carbon atoms of OCCO in turn to form DMO. The process of coupling of two CO molecules is accompanied by an activation barrier of 165.0 kJ mol⁻¹ (TS6) and a reaction energy of 153.2 kJ mol⁻¹. Obviously, the energy of the OCCO intermediate is only slightly lower (11.8 kJ mol⁻¹) than that of TS6, that is to say, the step is easily reversible and only when CO is pre-adsorbed and in excess, it is able to proceed to

the right. In the following step OCH_3 attacks one carbon atom of OCCO to form OCCOCH_3 , which needs an energy barrier of 31.2 kJ mol^{-1} . Finally, the other OCH_3 approaches to the adsorbed OCCOCH_3 to form DMO *via* TS5, which is the same as the third step of Path2. In summary, the Path3 has a higher C–C coupling barrier than Path1 and Path2.

As a result, the $\text{COOCH}_3\text{--COOCH}_3$ coupling is the favorable pathway for CO oxidation to DMO on the Pd(111) surface. In addition, the mechanism of CO oxidative coupling to DMO has also been investigated using *in situ* infrared spectroscopy. The ON-Pd-COOCH_3 intermediate was identified and the mechanism of DMO formation was proposed *via* two ON-Pd-COOCH_3 intermediates coupling to each other.¹⁵ Moreover, the Guo group¹¹ identified the $\text{CH}_3\text{OCO-Pd-COOCH}_3$ intermediate using the *in situ* diffuse reflectance infrared spectra, which indicated that the $\text{CH}_3\text{OCO-Pd-COOCH}_3$ intermediate quickly formed in the intramolecular coupling, resulting in the formation of DMO. Therefore, our DFT calculation is in good agreement with the previous experimental results. Additionally, DMC formation must overcome an energy barrier of $153.5 \text{ kJ mol}^{-1}$, which is higher than the energy barrier of $\text{COOCH}_3\text{--COOCH}_3$ coupling to DMO, indicating that it is very difficult for CO oxidation to DMC on the Pd(111) surface. It is well consistent with the results of the *in situ* DRIR spectra and space-time yield.^{7,11,12,15}

3.2.2 Reaction pathways for CO oxidative coupling to DMO on the Pd–Cu(111) surface. Similarly, the co-adsorption of CO and OCH_3 initiates the reaction of CO oxidative coupling to DMO on the Pd–Cu(111) surface, as shown in Fig. 7. In Path1, the adsorbed OCH_3 and CO obliquely bind to the two adjacent top site, then COOCH_3 is formed by the adsorbed OCH_3 through its oxygen attacking the carbon of nearby adsorbed CO *via* a transition state (TS1), which is accompanied by a little activation barrier of 15.6 kJ mol^{-1} and an exothermic energy of 87.5 kJ mol^{-1} . In TS1, the distance between the O atom of OCH_3 and the C atom of CO shortens to 2.267 from 3.032 \AA in IS1.

On the basis of the adsorption of the formed COOCH_3 , the other CO is adsorbed at the adjacent fcc site through C atoms, and the other OCH_3 occupies the bridge site through O atoms. The other COOCH_3 is formed through a transition state TS2, where the distance between the O atom of OCH_3 and the C atom of CO decreases to 2.093 from 3.473 \AA . This step is exothermic by 25.7 kJ mol^{-1} with an energy barrier of 45.6 kJ mol^{-1} , finally resulting in the formation of two COOCH_3 intermediates (IS3) with a C3–O4 bond length of 1.347 \AA . Two COOCH_3 coupling to DMO with a C1–C3 bond length of 1.541 \AA *via* a transition state (TS3) must overcome a high energy barrier of $132.2 \text{ kJ mol}^{-1}$, and it is exothermic (34.1 kJ mol^{-1}). In TS3, the distance between C1 and C3 atoms of two COOCH_3 is reduced from 3.288 to 2.026 \AA .

Additionally, the first reaction step of Path2 is the same as that of Path1. The COOCH_3 formed attacks CO which occupies on the fcc site to form OCCOCH_3 with a C1–C3 bond length of 1.545 \AA . Then, OCH_3 which sits at the bridge site approaches the carbon of OCCOCH_3 to form DMO. The C–C coupling process is accompanied by endothermic heat of 84.3 kJ mol^{-1} with a high barrier by $151.5 \text{ kJ mol}^{-1}$ (TS4), and the formation of DMO with OCCOCH_3 and OCH_3 must overcome a higher

barrier of $166.1 \text{ kJ mol}^{-1}$ and it is exothermic ($130.2 \text{ kJ mol}^{-1}$). In TS4, the distance between C1 and C3 atoms of COOCH_3 and CO decreases from 3.526 to 1.912 \AA . Moreover, the distance of C3–O4 in TS5 shortens to 2.879 from 3.661 \AA .

As for DMO synthesis, the rate-determining steps of Path1 and Path2 on the Pd–Cu(111) surface are R3 and R5 with an energy barrier of 132.2 and $166.1 \text{ kJ mol}^{-1}$, respectively, indicating that Path1 is a favorable pathway. However, DMC formation needs to surmount a high barrier of $194.8 \text{ kJ mol}^{-1}$, which indicates that it is unfavorable for CO oxidation to DMC. Additionally, the energy barrier of rate-determining steps of Path1 for DMO formation on the Pd–Cu(111) surface is higher (11.6 kJ mol^{-1}) than that on the Pd(111) surface. Accordingly, the catalytic activity of the Pd–Cu(111) surface is lower than that of the Pd(111) surface.

3.2.3 Reaction pathways for CO oxidative coupling to DMO on the Pd–Al(111) surface. It is the same as that on Pd(111) and Pd–Cu(111) surfaces, Path1 also starts from the co-adsorption of CO and OCH_3 on the Pd–Al(111) surface, where the adsorbed OCH_3 is obliquely adsorbed at a top site and meantime CO vertically binds to the adjacent top site, as shown in Fig. 8. Then, the O atom of OCH_3 approaches the carbon of nearby adsorbed CO to form COOCH_3 with a C1–O2 bond length of 1.368 \AA *via* a transition state TS1, where the distance between the O atom of OCH_3 and the C atom of CO decreases to 2.265 from 3.167 \AA in IS1. This step is exothermic with an energy of 34.8 kJ mol^{-1} and a little energy barrier of 19.6 kJ mol^{-1} .

The other COOCH_3 is formed along IS2–TS2–IS3, which has an activation barrier and a small reaction energy of 38.5 and -1.1 kJ mol^{-1} , respectively, finally leading to the formation of two COOCH_3 (intermediate state, IS3) with a C3–O4 bond length of 1.410 \AA . In IS2, the COOCH_3 formed occupies the top site through the C1 atom, CO binds to the adjacent top site through the C atom, and OCH_3 occupies the bridge site through the O atom. In TS2, the distance between the O atom of OCH_3 and the C atom of CO shortens to 2.129 from 3.367 \AA . The following coupling process of IS3 must surmount a high energy barrier (96.4 kJ mol^{-1}) *via* a transition state (TS3), and is exothermic by 35.1 kJ mol^{-1} to DMO with a C1–C3 bond length of 1.539 \AA . In TS3, the distance between C1 and C3 atoms of two COOCH_3 is decreased to 2.003 from 3.528 \AA .

To summarize, R3 is the rate-determining step with an energy barrier of 96.4 kJ mol^{-1} in Path1 on the Pd–Al(111) surface, which is lower (24.2 and 35.8 kJ mol^{-1} , respectively) than that on Pd(111) and Pd–Cu(111) surfaces. As a result, the Pd–Al(111) surface exhibits a higher catalytic activity in Path1.

The first reaction step of Path2 is just as that of Path1. The second step is COOCH_3 attacks CO which obliquely occupies on the adjacent top site to form OCCOCH_3 with a C1–C3 bond length of 1.543 \AA *via* a transition state (TS4), where the distance between C1 and C3 atoms decreases to 1.887 from 3.602 \AA . This process is accompanied by an endothermic heat of 43.3 kJ mol^{-1} with an energy barrier of $113.0 \text{ kJ mol}^{-1}$. In the last step, DMO is formed by OCH_3 which occupies on the fcc site attacking on the carbon of OCCOCH_3 *via* a transition state TS5, which is exothermic (83.0 kJ mol^{-1}) with an energy barrier of 42.0 kJ mol^{-1} . In TS5, the C3–O4 distance shortens from 4.417 to 2.120 \AA .

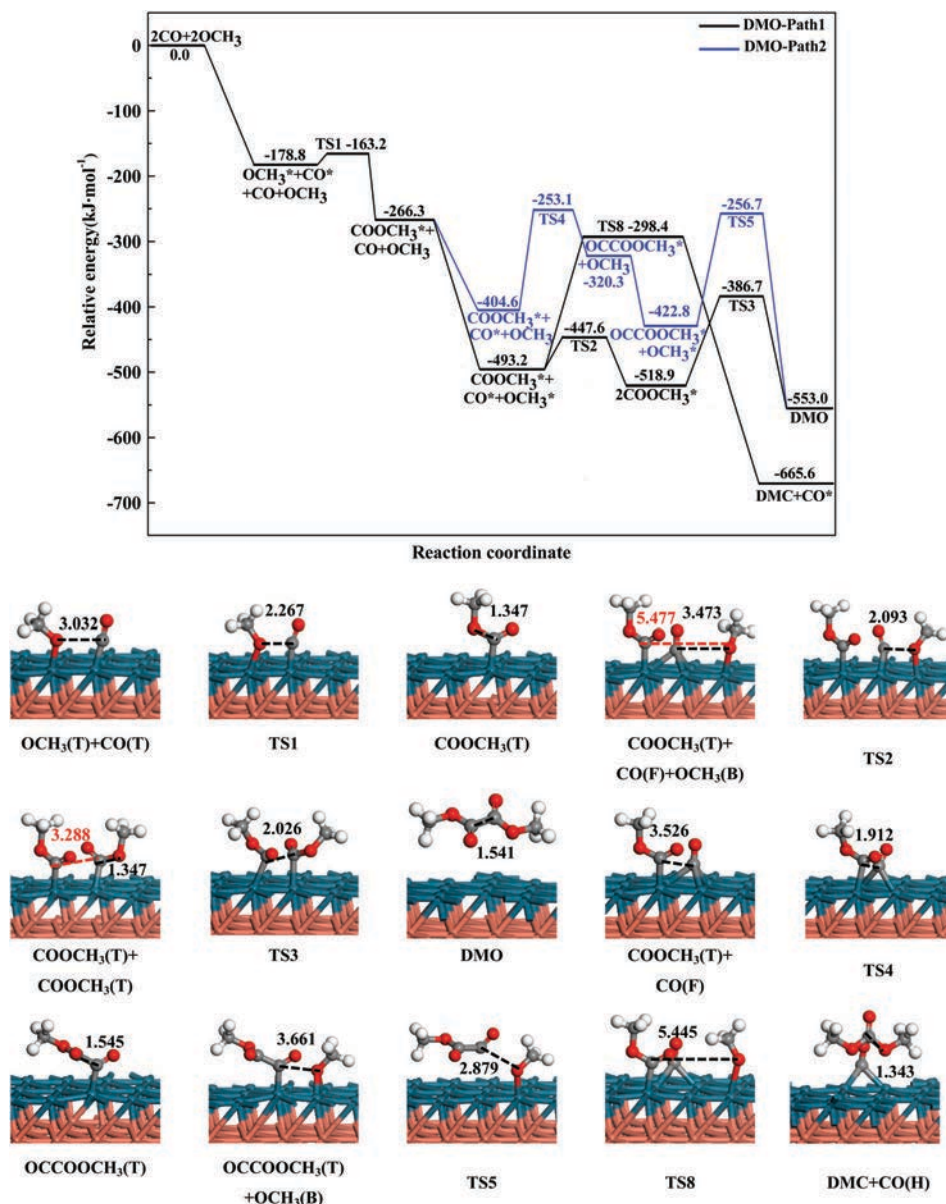


Fig. 7 Potential energy diagram of CO oxidative coupling to DMO and the corresponding configuration of initial states, transition states and final states on the Pd-Cu(111) surface.

In summary, the rate-determining step is R4 with an energy barrier of $113.0 \text{ kJ mol}^{-1}$ in Path2. It is higher (16.6 kJ mol^{-1}) than that of Path1, indicating that Path1 is favorable on the Pd-Al(111) surface. However, it is lower (47.1 and 53.1 kJ mol^{-1} , respectively) than that of Path2 on Pd(111) and Pd-Cu(111) surfaces, which implies that the Pd-Al(111) surface is significantly superior to Pd(111) and Pd-Cu(111) surfaces with respect to catalytic activity for DMO formation in Path1 and Path2. In addition, DMC formation must overcome a high barrier of $349.1 \text{ kJ mol}^{-1}$, indicating that it is unable to proceed for CO oxidation to DMC on the Pd-Al(111) surface.

3.3 Micro-kinetic modeling

On the basis of the calculated potential energy, we also take a further step to estimate the rate of the overall reaction on each

system. Micro-kinetic modeling^{69–74} has been widely employed to investigate the activity and selectivity of the catalyst. For example, Liu *et al.*⁷⁰ have proved that the water dissociation was faster on Au and Cu nanoparticles than their parent bulk surfaces, which was the rate-determining step for the water-gas-shift reaction. Additionally, it was obtained that the selectivity of N_2 is higher than that of NH_3 for the NO reduction by H_2 on the stepped Pd(211) surface.⁷²

In this study, the micro-kinetic modeling is implemented to probe into the catalytic activity and selectivity for CO oxidative coupling to DMO on Pd(111), Pd-Cu(111) and Pd-Al(111) surfaces, where the surface coverage of all species and the generation rate of products are obtained. As CH_3ONO can easily dissociate into OCH_3 and NO ,^{7,8} and the generated NO desorbs directly⁹ or reacts quickly with methanol and oxygen to form

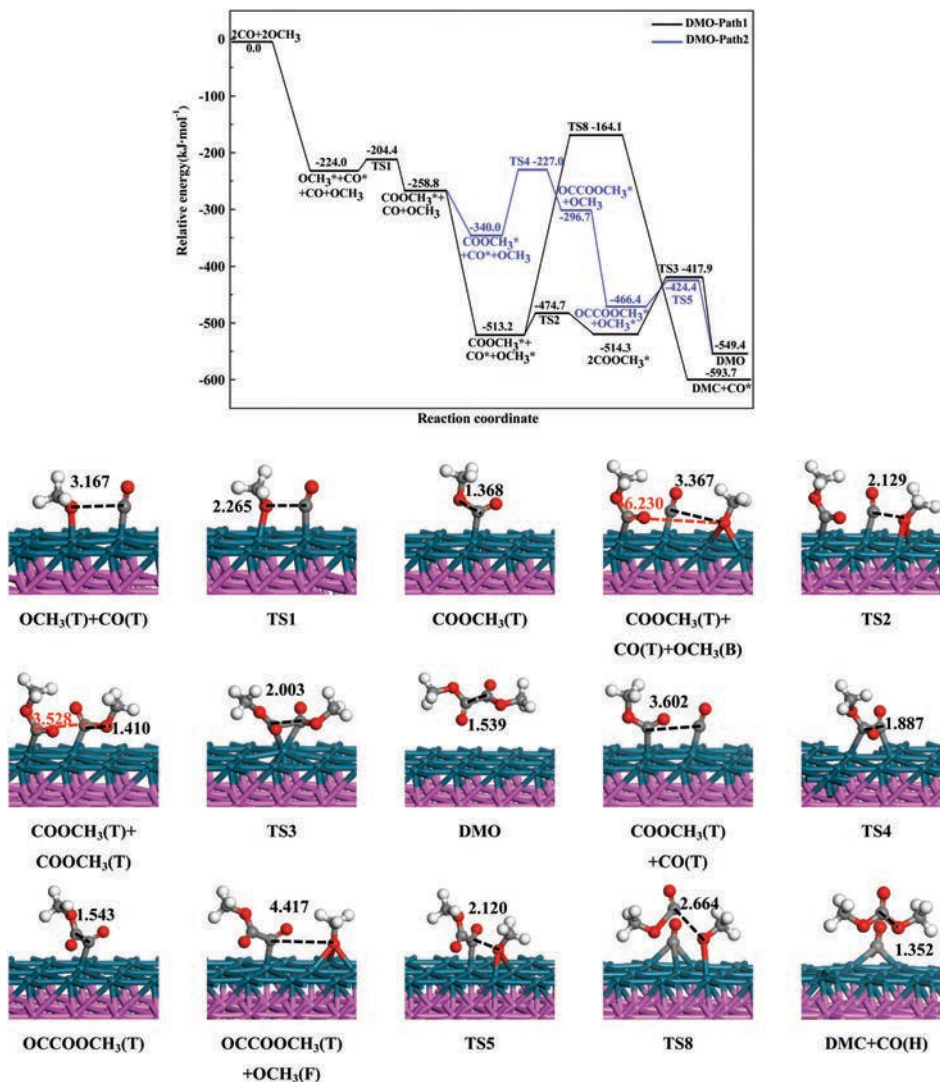


Fig. 8 Potential energy diagram of CO oxidative coupling to DMO and the corresponding configuration of initial states, transition states and final states on the Pd-Al(111) surface.

CH₃ONO without any catalyst,¹⁰ the coverage of CH₃ONO is not considered, and the pressure of OCH₃ is approximately equal to that of CH₃ONO. All possible reaction steps for the formation of DMO are listed in Table 2.

Rate constants for all elementary steps are calculated based on the harmonic transition state theory (TST)⁷⁵ in the following eqn (9):

$$k = v_i \exp\left(\frac{-E_a}{RT}\right) \quad (9)$$

where v_i is the pre-exponential factor, E_a is the ZPE-corrected energy barrier, and T is the temperature. The pre-exponential factor v_i of each reaction is calculated by the following eqn (10):⁷⁶

$$v_i = \frac{k_B T}{h} \frac{\prod_{i=1}^{3N} \left[1 - \exp\left(-\frac{hf_i^{IS}}{k_B T}\right)\right]}{\prod_{i=1}^{3N-1} \left[1 - \exp\left(-\frac{hf_i^{TS}}{k_B T}\right)\right]} \quad (10)$$

Table 2 The related reactions and the representation of the corresponding rate constant

Reaction	Rate constant
$\text{CO}^* + \text{OCH}_3^* \rightarrow \text{COOCH}_3^*$	k_1
$\text{COOCH}_3^* + \text{CO}^* + \text{OCH}_3^* \rightarrow 2\text{COOCH}_3^* + *$	k_2
$2\text{COOCH}_3^* \rightarrow (\text{COOCH}_3)_2 + 2^*$	k_3
$\text{COOCH}_3^* + \text{CO}^* \rightarrow \text{OCCOOCH}_3^* + *$	k_4
$\text{OCCOOCH}_3^* + \text{OCH}_3^* \rightarrow (\text{COOCH}_3)_2 + 2^*$	k_5
$2\text{CO}^* \rightarrow \text{OCCO}^* + *$	k_6
$\text{OCCO}^* + \text{OCH}_3^* \rightarrow \text{OCCOOCH}_3^* + *$	k_7
$\text{COOCH}_3^* + \text{CO}^* + \text{OCH}_3^* \rightarrow \text{DMC} + \text{CO}^* + 2^*$	k_8

where f_i^{IS} are the vibrational frequencies at the initial state and f_i^{TS} are the vibrational frequencies at the transition state (excluding the imaginary one). Additionally, k_B is the Boltzmann constant.

The site balance of the intermediate species involved in the reaction and free site (*) can be written as follows:

$$\theta_{\text{CO}} + \theta_{\text{OCH}_3} + \theta_{\text{COOCH}_3} + \theta_{\text{OCCOOCH}_3} + \theta_{\text{OCCO}} + \theta^* = 1 \quad (11)$$

The coverage of surface OCH_3 and CO is obtained by the following formulas (12) and (13):

$$\theta_{\text{OCH}_3} = P_{\text{OCH}_3} K_{\text{OCH}_3} \theta^* \quad (12)$$

$$\theta_{\text{CO}} = P_{\text{CO}} K_{\text{CO}} \theta^* \quad (13)$$

The adsorption process of OCH_3 and CO is also assumed to be in equilibrium and the equilibrium constant K_{eq} is estimated according to eqn (14):

$$K_{\text{eq}} = \exp[-(\Delta E_{\text{ads}} - T\Delta S)/RT] \quad (14)$$

where ΔE_{ads} is the adsorption energy of OCH_3 and CO , respectively. ΔS is the entropy change of OCH_3 and CO induced by adsorption, respectively. It can be obtained by the following eqn (15) and (16):⁷⁷

$$\Delta S = S_{\text{adsorbate}} - S_{\text{gas}} \quad (15)$$

$$S = R \sum_{i=1}^{3N} \left[-\ln \left(1 - \exp \left(-\frac{hf_i}{k_B T} \right) \right) + \frac{hf_i}{k_B T} \frac{\exp \left(-\frac{hf_i}{k_B T} \right)}{1 - \exp \left(-\frac{hf_i}{k_B T} \right)} \right] \quad (16)$$

where $S_{\text{adsorbate}}$ is the entropy of OCH_3 and CO adsorbing on Pd(111), Pd-Cu(111) and Pd-Al(111) surfaces, and S_{gas} is the gas phase entropy. Typical experimental conditions¹¹ ($P_{\text{CH}_3\text{ONO}} = 200$ kPa, $P_{\text{CO}} = 280$ kPa and $T = 375$ – 415 K) are adopted.

The coverage of other surface species can be described according to the steady-state approximation, where rates for

the production and the consumption of each species were assumed to be equal:

$$\theta_{\text{COOCH}_3} : \frac{d\theta_{\text{COOCH}_3}}{dt} = k_1 \theta_{\text{OCH}_3} \theta_{\text{CO}} + k_2 \theta_{\text{OCH}_3} \theta_{\text{CO}} - k_3 \theta_{\text{COOCH}_3}^2 - k_4 \theta_{\text{COOCH}_3} \theta_{\text{CO}} - k_8 \theta_{\text{COOCH}_3} \theta_{\text{OCH}_3} = 0 \quad (17)$$

$$\theta_{\text{OCCOOCH}_3} : \frac{d\theta_{\text{OCCOOCH}_3}}{dt} = k_4 \theta_{\text{COOCH}_3} \theta_{\text{CO}} + k_7 \theta_{\text{OCCO}} \theta_{\text{OCH}_3} - k_5 \theta_{\text{OCCOOCH}_3} \theta_{\text{OCH}_3} = 0 \quad (18)$$

$$\theta_{\text{OCCO}} : \frac{d\theta_{\text{OCCO}}}{dt} = k_6 \theta_{\text{CO}}^2 - k_7 \theta_{\text{OCCO}} \theta_{\text{OCH}_3} = 0 \quad (19)$$

The rate constants for all elementary steps and entropy change of OCH_3 and CO in the temperature range of 375–415 K are shown in Table 3. The favorable pathways for CO oxidation to DMO on these catalysts are obtained from the analysis of rate constants. The DMO formation is mainly contributed by the COOCH_3 – COOCH_3 coupling route on these catalysts. Compared with the rate constant of each elementary step in their pathways, $2\text{COOCH}_3 \rightarrow (\text{COOCH}_3)_2$, $\text{COOCH}_3 + \text{CO} \rightarrow \text{OCCOOCH}_3$ and $2\text{CO} \rightarrow \text{OCCO}$ are the rate-determining steps for DMO formation in Path1, Path2 and Path3, respectively, except that $\text{OCCOOCH}_3 + \text{CO} \rightarrow (\text{COOCH}_3)_2$ is in Path2 on the Pd-Cu(111) surface. In addition, the rate constants for DMO generation are far higher than those for DMC formation on

Table 3 The reaction equilibrium constants and rate constants k (s^{-1}) ($375 \text{ K} \leq T \leq 415 \text{ K}$)

		Equilibrium constants/rate constants				
		375 K	385 K	395 K	405 K	415 K
Pd(111)	K_{CO}	5.50×10^{13}	1.81×10^{13}	6.32×10^{12}	2.32×10^{12}	8.95×10^{11}
	K_{OCH_3}	2.79×10^{16}	1.28×10^{16}	4.08×10^{15}	1.37×10^{15}	4.87×10^{14}
	k_1	2.13×10^6	2.93×10^6	3.97×10^6	4.59×10^6	6.94×10^6
	k_2	2.52×10^4	3.89×10^4	5.87×10^4	7.16×10^4	1.26×10^5
	k_3	4.72×10^{-6}	1.29×10^{-5}	3.35×10^{-5}	5.31×10^{-5}	1.98×10^{-4}
	k_4	1.54×10^{-10}	5.92×10^{-10}	2.12×10^{-9}	3.92×10^{-9}	2.27×10^{-8}
	k_5	4.03×10^8	5.28×10^8	6.81×10^8	7.70×10^8	1.09×10^9
	k_6	2.94×10^{-11}	1.17×10^{-10}	4.32×10^{-10}	8.12×10^{-10}	4.91×10^{-9}
Pd-Cu(111)	k_7	1.49×10^9	1.98×10^9	2.60×10^9	2.96×10^9	4.30×10^9
	k_8	1.43×10^{-9}	5.23×10^{-9}	1.79×10^{-8}	5.79×10^{-8}	1.77×10^{-7}
	K_{CO}	2.15×10^6	1.10×10^6	5.81×10^5	3.17×10^5	1.78×10^5
	K_{OCH_3}	1.48×10^{11}	6.14×10^{10}	2.67×10^{10}	1.21×10^{10}	5.69×10^9
	k_1	4.70×10^9	5.36×10^9	6.07×10^9	6.83×10^9	8.20×10^9
	k_2	7.10×10^5	1.04×10^6	1.51×10^6	2.14×10^6	3.05×10^6
	k_3	7.92×10^{-7}	2.42×10^{-6}	6.98×10^{-6}	1.91×10^{-5}	2.71×10^{-5}
	k_4	8.34×10^{-9}	3.00×10^{-8}	1.01×10^{-7}	3.22×10^{-7}	4.10×10^{-7}
Pd-Al(111)	k_5	1.27×10^{-9}	5.23×10^{-9}	2.00×10^{-8}	7.15×10^{-8}	1.03×10^{-7}
	k_8	1.98×10^{-14}	1.05×10^{-13}	5.10×10^{-13}	2.30×10^{-12}	3.41×10^{-12}
	K_{CO}	1.63×10^6	8.39×10^5	4.46×10^5	2.45×10^5	1.38×10^5
	K_{OCH_3}	4.35×10^{16}	1.35×10^{16}	4.47×10^{15}	1.56×10^{15}	5.71×10^{14}
	k_1	2.01×10^{10}	2.38×10^{10}	2.79×10^{10}	3.26×10^{10}	3.77×10^{10}
	k_2	1.85×10^7	2.57×10^7	3.51×10^7	4.73×10^7	6.28×10^7
	k_3	6.69×10^{-2}	1.50×10^{-1}	3.22×10^{-1}	6.66×10^{-1}	1.33
	k_4	8.13×10^{-4}	2.11×10^{-3}	5.21×10^{-3}	1.23×10^{-2}	2.79×10^{-2}
Pd-Al(111)	k_5	1.06×10^6	1.50×10^6	2.08×10^6	2.86×10^6	3.85×10^6
	k_8	1.24×10^{-33}	2.47×10^{-32}	4.22×10^{-31}	6.28×10^{-30}	8.21×10^{-29}

Table 4 The surface coverage of different species (375 K ≤ T ≤ 415 K)

		375 K	385 K	395 K	405 K	415 K
Pd(111)	θ^*	5.04×10^{-27}	1.83×10^{-26}	7.60×10^{-26}	2.53×10^{-25}	1.07×10^{-24}
	θ_{CO}	7.76×10^{-8}	9.27×10^{-8}	1.35×10^{-7}	1.64×10^{-7}	2.68×10^{-7}
	θ_{OCH_3}	2.81×10^{-5}	4.68×10^{-5}	6.20×10^{-5}	6.94×10^{-5}	1.04×10^{-4}
	θ_{COOCH_3}	1.00	1.00	1.00	1.00	1.00
	$\theta_{\text{OCCOOCH}_3}$	1.06×10^{-21}	2.22×10^{-21}	6.76×10^{-21}	1.21×10^{-20}	5.33×10^{-20}
	θ_{OCCO}	4.22×10^{-30}	1.08×10^{-29}	4.86×10^{-29}	1.07×10^{-28}	7.88×10^{-28}
Pd-Cu(111)	θ^*	9.73×10^{-23}	3.46×10^{-22}	1.15×10^{-21}	3.61×10^{-21}	7.63×10^{-21}
	θ_{CO}	5.87×10^{-11}	1.06×10^{-10}	1.87×10^{-10}	3.20×10^{-10}	3.80×10^{-10}
	θ_{OCH_3}	2.87×10^{-6}	4.24×10^{-6}	6.15×10^{-6}	8.74×10^{-6}	8.68×10^{-6}
	θ_{COOCH_3}	1.00	1.00	1.00	1.00	1.00
	$\theta_{\text{OCCOOCH}_3}$	1.34×10^{-4}	1.44×10^{-4}	1.54×10^{-4}	1.65×10^{-4}	1.74×10^{-4}
	Pd-Al(111)	θ^*	2.31×10^{-23}	7.83×10^{-23}	2.49×10^{-22}	7.50×10^{-22}
θ_{CO}		1.06×10^{-11}	1.84×10^{-11}	3.12×10^{-11}	5.14×10^{-11}	6.29×10^{-11}
θ_{OCH_3}		2.01×10^{-1}	2.12×10^{-1}	2.23×10^{-1}	2.34×10^{-1}	2.86×10^{-1}
θ_{COOCH_3}		7.99×10^{-1}	7.88×10^{-1}	7.77×10^{-1}	7.66×10^{-1}	7.14×10^{-1}
$\theta_{\text{OCCOOCH}_3}$		3.23×10^{-20}	9.62×10^{-20}	2.71×10^{-19}	7.27×10^{-19}	1.14×10^{-18}

these catalysts, which implies that CO oxidation to DMC is difficult.

From eqn (17)–(19), the coverage of all reactive species can be obtained, as shown in Table 4. The results indicate that coverage of COOCH₃ is approximately equal to 0.71–1.00, and much greater than that of other species on these catalysts, because the other species are involved in the reactions whose energy barriers are relatively lower, and they can be quickly consumed. The similar results have been obtained in the reaction of reduction of NO,⁷² where the micro-kinetic modeling results indicated that NO coverage was about 0.99 owing to NO participating in rate-determining steps, whereas the sum of the coverage of other species was close to 0.01. In addition, the COOCH₃ coverage on the Pd–Al(111) surface is lower than that on Pd(111) and Pd–Cu(111) surfaces. Relatively lower energy barriers of rate-determining steps on the Pd–Al(111) surface make COOCH₃ species relatively easily participate in the following reactions.

The formation rate of one product is proportional to the concentration of reactants and the reaction rate constant.⁷⁸ Therefore, the formation rates of DMO and DMC are expressed as the following formula:

$$r_{\text{DMO}} = k_3\theta_{\text{COOCH}_3}^2 + k_5\theta_{\text{OCCOOCH}_3}\theta_{\text{OCH}_3} \quad (20)$$

$$r_{\text{DMC}} = k_8\theta_{\text{COOCH}_3}\theta_{\text{OCH}_3} \quad (21)$$

The formation rate of DMO and DMC in the temperature range of 375–415 K is shown in Table 5. The results show that

the rate of DMO generation is far higher than that of DMC formation and the selectivity towards DMO is close to 100% on these catalysts, where the selectivity of DMO on Pd(111) surface is in well agreement with the experiment that it is approximately equal to 100% and remains constant in the range of 375–415 K on Pd nanocatalysts dominated by the (111) facet,¹¹ as well as 99.6–100% at 363–413 K.⁷ Additionally, the rate of DMO generation follows the trend of Pd–Al(111) > Pd(111) > Pd–Cu(111), which is in good agreement with the results of analysis of activation energy barriers and rate constants.

3.4 General discussion

According to the above results, it is clear that the mechanism of CO oxidation on Pd(111), Pd–Cu(111) and Pd–Al(111) surfaces has priority to follow the COOCH₃–COOCH₃ coupling pathway and the catalytic activity of these catalysts abides by the trend of Pd–Al(111) > Pd(111) > Pd–Cu(111). In Path1, the complex of two COOCH₃ intermediates formed firstly, followed by the coupling of two COOCH₃ to form DMO. It is obvious that the C–C coupling step is the rate-determining step, of which the energy barrier on the Pd–Al(111) surface is lower (24.2 kJ mol⁻¹ and 35.8 kJ mol⁻¹) than that on Pd(111) and Pd–Cu(111) surfaces, respectively. When CO oxidation to DMO occurs along the Path2, it is difficult to accomplish coupling of COOCH₃ and CO on these catalysts. Additionally, OCH₃ approaching OCCOOCH₃ also needs to overcome a higher energy barrier on the Pd–Cu(111) surface. In Path3, OCCO is easily decomposed to adsorb CO on the

Table 5 The formation rates (s⁻¹) of DMO and DMC (375 K ≤ T ≤ 415 K)

		375 K	385 K	395 K	405 K	415 K
Pd(111)	DMO	4.72×10^{-6}	1.29×10^{-5}	3.35×10^{-5}	5.31×10^{-5}	1.98×10^{-4}
	DMC	4.02×10^{-14}	2.45×10^{-13}	1.11×10^{-12}	4.02×10^{-12}	6.04×10^{-12}
Pd–Cu(111)	DMO	7.92×10^{-7}	2.42×10^{-6}	6.98×10^{-6}	1.91×10^{-5}	2.71×10^{-5}
	DMC	5.67×10^{-20}	4.44×10^{-19}	3.14×10^{-18}	2.01×10^{-17}	2.96×10^{-17}
Pd–Al(111)	DMO	4.27×10^{-2}	9.29×10^{-2}	1.94×10^{-1}	3.91×10^{-1}	6.79×10^{-1}
	DMC	1.99×10^{-34}	4.12×10^{-33}	7.31×10^{-32}	1.12×10^{-30}	1.68×10^{-29}

Pd(111) surface, therefore, the reaction is difficult to proceed to the right. Additionally, the energy barrier for DMC formation is far higher than that for DMO formation on these catalysts, indicating that Pd–Cu and Pd–Al bimetallic catalysts possess high selectivity for DMO formation. The micro-kinetic modeling is employed to probe into the catalytic activity and selectivity of these catalysts, and the result is in agreement with the results of energy barrier analysis.

It has been well established that catalytic activity of a bimetallic catalyst is attributed to the strain subjected to the surface (strain effect) and the electronic structure change of the outermost metal caused by the substrates (ligand effect).^{79–81} The strain effect of substrate Cu or Al subjected to the Pd surface, and the ligand effect of the electronic structure change of the outermost Pd caused by the substrate lead to the change of the catalytic activity of Pd–Cu(111) and Pd–Al(111) relative to the pure Pd(111) surface. Therefore, we investigated strain and ligand effects on the activation energy barrier of the rate-determining step in a favorable reaction path on Pd–Cu(111) and Pd–Al(111) surfaces. The strain contribution ($\Delta E_a^{\text{strain}}$), the ligand contribution ($\Delta E_a^{\text{ligand}}$) and the total contribution ($\Delta E_a^{\text{total}}$) are defined using the following eqn (22)–(24),^{82,83} respectively:

$$\Delta E_a^{\text{strain}} = E_a^{\text{strain-M}} - E_a(\text{Pd}) \quad (22)$$

$$\Delta E_a^{\text{ligand}} = E_a(\text{Pd-M}) - E_a^{\text{strain-M}} \quad (23)$$

$$\Delta E_a^{\text{total}} = \Delta E_a^{\text{strain}} + \Delta E_a^{\text{ligand}} \quad (24)$$

where, $E_a^{\text{strain-M}}$ is the activation energy barrier on the strained monometallic Pd surface with the same lattice constant as the corresponding Pd–M(111) surfaces; $E_a(\text{Pd})$ and $E_a(\text{Pd-M})$ are activation energy barriers on Pd(111) and Pd–M(111) surfaces, respectively. In addition, the positive value indicates that the catalytic activity is decreased, whereas negative value shows that it is increased.

Relative contribution of strain and ligand effects in the activation energy barrier of $2\text{COOCH}_3 \rightarrow \text{DMO}$ on Pd–Cu(111) and Pd–Al(111) surfaces is shown in Table 6. It can be seen that the strain effect reduces the activation energy barrier, whereas the ligand effect increases it on Pd–Cu(111) and Pd–Al(111) surfaces. The contribution of the strain effect is weaker than that of the ligand effect on the Pd–Cu(111) surface, which leads to an increase in the activation energy barrier, thereby decreasing the catalytic activity for CO oxidation to DMO. The same result was also obtained for the selective H_2 formation by HCOOH decomposition. The catalytic activity of Pd–Ir(111) is lower than that of the Pd(111) surface, in which the contribution of the strain effect (decreasing energy barrier) is weaker than that of the ligand effect (increasing energy barrier) on the

Table 6 Relative contribution of strain and ligand effects to the activation energy barrier (kJ mol^{-1}) of $2\text{COOCH}_3 \rightarrow \text{DMO}$ on Pd–Cu(111) and Pd–Al(111) surfaces

	$E_a^{\text{strain-M}}$	$\Delta E_a^{\text{strain}}$	$\Delta E_a^{\text{ligand}}$	$\Delta E_a^{\text{total}}$
Pd–Cu(111)	93.7	–26.9	38.5	11.6
Pd–Al(111)	71.2	–49.4	25.2	–24.2

Pd–Ir(111) surface.⁸³ Whereas, the contribution of the strain effect is stronger than that of ligand effects on the Pd–Al(111) surface for DMO formation, thereby improving its catalytic activity.

4. Conclusions

In the present work, we combined DFT calculations and micro-kinetic modeling to study the reaction mechanism of CO oxidative coupling to DMO on Pd(111), Pd–Cu(111) and Pd–Al(111) surfaces. Our DFT results show that Pd–Cu and Pd–Al bimetallic catalysts possess high stability. Additionally, the C–C coupling elementary reaction is the rate-determining step the rate-determining step in each pathway on these catalysts, except that OCH_3 attacking OCCOCH_3 is in Path2 on the Pd–Cu(111) surface. The favorable pathway for this process is the COOCH_3 – COOCH_3 coupling route, and the catalytic activity of these catalysts follows the order of Pd–Al(111) > Pd(111) > Pd–Cu(111). Additionally, CO oxidation to DMC is difficult to perform on these catalysts, which needs to overcome a very higher energy barrier than for DMO formation. Furthermore, the micro-kinetic modeling result demonstrates that the generation rate of DMO on these catalysts in the appropriate temperature range of 375–415 K is consistent with the results of energy barrier analysis. It can be concluded that the Pd–Al bimetallic catalyst can effectively enhance the catalytic performance and reduce the cost for CO oxidative coupling to DMO. It is also believed that the insights derived from this study can provide a clue for designing high-efficient and low-cost bimetallic catalysts.

Conflicts of interest

There are no conflicts to declare.

Acknowledgements

We gratefully acknowledge financial support from the National Natural Science Foundation of China (Grant No. 21576178 and 21476155), the Key Projects of National Natural Science Foundation of China (21736007), Research Project Supported by Shanxi Scholarship Council of China (No. 2016-030) and the Foundation of State Key Laboratory of Coal Conversion (No. J18-19-602).

References

- L. F. Chen, P. J. Guo, M. H. Qiao, S. R. Yan, H. X. Li, W. Shen, H. L. Xu and K. N. Fan, *J. Catal.*, 2008, **257**, 172–180.
- A. Y. Yin, X. Y. Guo, W. L. Dai and K. N. Fan, *Chem. Commun.*, 2010, **46**, 4348–4350.
- Z. He, H. Q. Lin, P. He and Y. Z. Yuan, *J. Catal.*, 2011, **277**, 54–63.
- J. Ding, T. Popa, J. K. Tang, K. A. M. Gasem, M. H. Fan and Q. Zhong, *Appl. Catal., B*, 2017, **209**, 530–542.

- 5 Y. J. Zhao, Y. Q. Zhang, Y. Wang, J. Zhang, Y. Xu, S. P. Wang and X. B. Ma, *Appl. Catal., A*, 2017, **539**, 59–69.
- 6 D. M. Fenton and P. J. Steinwand, *J. Org. Chem.*, 1974, **39**, 701–704.
- 7 Q. H. Li, Z. F. Zhou, R. P. Chen, B. Z. Sun, L. Y. Qiao, Y. G. Yao and K. C. Wu, *Phys. Chem. Chem. Phys.*, 2015, **17**, 9126–9134.
- 8 C. Fan, M. Luo and W. D. Xiao, *Chin. J. Chem. Eng.*, 2016, **24**, 132–139.
- 9 C. Z. Wang, P. J. Chen, Y. K. Li, G. F. Zhao, Y. Liu and Y. Lu, *J. Catal.*, 2016, **344**, 173–183.
- 10 F. D. Meng, G. H. Xu, R. Q. Guo, H. F. Yan and M. Q. Chen, *Chem. Eng. Process.*, 2004, **43**, 785–790.
- 11 Z. N. Xu, J. Sun, C. S. Lin, X. M. Jiang, Q. S. Chen, S. Y. Peng, M. S. Wang and G. C. Guo, *ACS Catal.*, 2013, **3**, 118–122.
- 12 S. Y. Peng, Z. N. Xu, Q. S. Chen, Y. M. Chen, J. Sun, Z. Q. Wang, M. S. Wang and G. C. Guo, *Chem. Commun.*, 2013, **49**, 5718–5720.
- 13 X. G. Zhao, Q. Lin and W. D. Xiao, *Appl. Catal., A*, 2005, **284**, 253–257.
- 14 Q. Lin, Y. Ji, Z. D. Jiang and W. D. Xiao, *Ind. Eng. Chem. Res.*, 2007, **46**, 7950–7954.
- 15 Y. Ji, G. Liu, W. Li and W. D. Xiao, *J. Mol. Catal. A: Chem.*, 2009, **314**, 63–70.
- 16 S. Y. Peng, Z. N. Xu, Q. S. Chen, Z. Q. Wang, Y. M. Chen, D. M. Lv, G. Lu and G. C. Guo, *Catal. Sci. Technol.*, 2014, **4**, 1925–1930.
- 17 E. L. Jin, L. L. He, Y. L. Zhang, A. R. Richard and M. H. Fan, *RSC Adv.*, 2014, **4**, 48901–48904.
- 18 S. Y. Peng, Z. N. Xu, Q. S. Chen, Z. Q. Wang, D. M. Lv, J. Sun, Y. M. Chen and G. C. Guo, *ACS Catal.*, 2015, **5**, 4410–4417.
- 19 H. L. Jiang and Q. Xu, *J. Mater. Chem.*, 2011, **21**, 13705–13725.
- 20 W. T. Yu, M. D. Porosoff and J. G. Chen, *Chem. Rev.*, 2012, **112**, 5780–5817.
- 21 R. Ferrando, J. Jellinek and R. L. Johnston, *Chem. Rev.*, 2008, **108**, 845–910.
- 22 D. S. Wang and Y. D. Li, *Adv. Mater.*, 2011, **23**, 1044–1060.
- 23 J. L. Shi, *Chem. Rev.*, 2013, **113**, 2139–2181.
- 24 J. K. Nørskov, T. Bligaard, J. Rossmeisl and C. H. Christensen, *Nat. Chem.*, 2009, **1**, 37–46.
- 25 P. Strasser, S. Koh, T. Anniyev, J. Greeley, K. More, C. F. Yu, Z. C. Liu, S. Kaya, D. Nordlund, H. Ogasawara, M. F. Toney and A. Nilsson, *Nat. Chem.*, 2010, **2**, 454–460.
- 26 G. Prieto, S. Beijer, M. L. Smith, M. He, Y. E. Au, Z. Wang, D. A. Bruce, K. P. D. Jong, J. J. Spivey and P. E. D. Jongh, *Angew. Chem., Int. Ed.*, 2014, **53**, 6397–6401.
- 27 Y. Z. Xiang and N. Kruse, *Nat. Commun.*, 2016, **7**, 13058.
- 28 M. S. Kumara, D. Chen, A. Holmen and J. C. Walmsley, *Catal. Today*, 2009, **142**, 17–23.
- 29 E. Y. Ko, E. D. Park, H. C. Lee, D. Lee and S. Kim, *Angew. Chem., Int. Ed.*, 2007, **46**, 734–737.
- 30 O. M. Ilinitch, L. V. Nosova, V. V. Gorodetskii, V. P. Ivanov, S. N. Trukhan, E. N. Gribov, S. V. Bogdanov and F. P. Cuperus, *J. Mol. Catal. A: Chem.*, 2000, **158**, 237–249.
- 31 S. L. Shen, J. Zhuang, Y. Yang and X. Wang, *Nanoscale*, 2011, **3**, 272–279.
- 32 X. Y. Liu, A. Q. Wang, X. D. Wang, C. Y. Mou and T. Zhang, *Chem. Commun.*, 2008, 3187–3189.
- 33 L. P. Shen, H. Z. Li, L. Lu, Y. F. Luo, Y. W. Tang, Y. Chen and T. H. Lu, *Electrochim. Acta*, 2013, **89**, 497–502.
- 34 G. N. Jovanovic, P. Ž. Plazl, P. Sakrithichai and K. Al-Khaldi, *Ind. Eng. Chem. Res.*, 2005, **44**, 5099–5106.
- 35 B. W. Zhu and T. T. Lim, *Environ. Sci. Technol.*, 2007, **41**, 7523–7529.
- 36 S. Agarwal, S. R. Al-Abed and D. D. Dionysiou, *Environ. Sci. Technol.*, 2007, **41**, 3722–3727.
- 37 K. Tedsree, T. Li, S. Jones, C. W. A. Chan, K. M. K. Yu, P. A. J. Bagot, E. A. Marquis, G. D. W. Smith and S. C. E. Tsang, *Nat. Nanotechnol.*, 2011, **6**, 302–307.
- 38 Y. C. Zhao, X. L. Yang, J. N. Tian, F. Y. Wang and L. Zhan, *Int. J. Hydrogen Energy*, 2010, **35**, 3249–3257.
- 39 M. H. Shao, K. Sasaki, N. S. Marinkovic, L. H. Zhang and R. R. Adzic, *Electrochem. Commun.*, 2007, **9**, 2848–2853.
- 40 G. Kyriakou, M. B. Boucher, A. D. Jewell, E. A. Lewis, T. J. Lawton, A. E. Baber, H. L. Tierney, M. Flytzani-Stephanopoulos and E. C. H. Sykes, *Science*, 2012, **335**, 1209–1212.
- 41 S. J. Li, D. J. Cheng, X. G. Qiu and D. P. Cao, *Electrochim. Acta*, 2014, **143**, 44–48.
- 42 B. Yang, S. B. Deng, G. Yu, H. Zhang, J. H. Wu and Q. F. Zhuo, *J. Hazard. Mater.*, 2011, **189**, 76–83.
- 43 B. Yang, S. B. Deng, G. Yu, Y. H. Lu, H. Zhang, J. Z. Xiao, G. Chen, X. B. Cheng and L. L. Shi, *Chem. Eng. J.*, 2013, **219**, 492–498.
- 44 J. A. Rodriguez, *Surf. Sci.*, 1994, **318**, 253–261.
- 45 L. Q. Jiang, M. W. Ruckman and M. Strongin, *Phys. Rev. B: Condens. Matter Mater. Phys.*, 1989, **39**, 1564–1568.
- 46 B. Frick and K. Jacobi, *Phys. Rev. B: Condens. Matter Mater. Phys.*, 1988, **37**, 4408–4414.
- 47 B. Frick and K. Jacobi, *Surf. Sci.*, 1986, **178**, 907–916.
- 48 B. Frick, K. Jacobi, J. A. Wilder, H. J. Sagner and K. H. Frank, *Surf. Sci.*, 1988, **193**, 529–533.
- 49 I. A. Pašti and S. V. Mentus, *Electrochim. Acta*, 2010, **55**, 1995–2003.
- 50 B. B. Xiao, Y. F. Zhu, X. Y. Lang, Z. Wen and Q. Jiang, *Sci. Rep.*, 2014, **4**, 5205.
- 51 G. Kresse and J. Furthmüller, *Comput. Mater. Sci.*, 1996, **6**, 15–50.
- 52 G. Kresse and J. Furthmüller, *Phys. Rev. B: Condens. Matter Mater. Phys.*, 1996, **54**, 11169–11186.
- 53 P. E. Blöchl, *Phys. Rev. B: Condens. Matter Mater. Phys.*, 1994, **50**, 17953–17979.
- 54 G. Kresse and D. Joubert, *Phys. Rev. B: Condens. Matter Mater. Phys.*, 1999, **59**, 1758–1775.
- 55 J. P. Perdew, K. Burke and M. Ernzerhof, *Phys. Rev. Lett.*, 1996, **77**, 3865–3868.
- 56 D. Sheppard, P. H. Xiao, W. Chemelewski, D. D. Johnson and G. Henkelman, *J. Phys. Chem.*, 2012, **136**, 074103.
- 57 D. Sheppard, R. Terrell and G. Henkelman, *J. Phys. Chem.*, 2008, **128**, 134106.
- 58 G. Henkelman and H. Jónsson, *J. Phys. Chem.*, 1999, **111**, 7010–7022.
- 59 R. A. Olsen, G. J. Kroes, G. Henkelman, A. Arnaldsson and H. Jónsson, *J. Phys. Chem.*, 2004, **121**, 9776–9792.

- 60 N. W. Ashcroft and N. D. Mermin, *Solid State Physics*, Saunders College Publishing, 1976.
- 61 T. Wang, X. X. Tian, Y. Yang, Y. W. Li, J. G. Wang, M. Beller and H. J. Jiao, *Phys. Chem. Chem. Phys.*, 2016, **18**, 6005–6012.
- 62 K. Li, H. Y. Liu, R. G. Zhang, L. X. Ling and B. J. Wang, *Appl. Surf. Sci.*, 2016, **390**, 7–16.
- 63 S. D. Miller and J. R. Kitchin, *Surf. Sci.*, 2009, **603**, 794–801.
- 64 L. A. Kibler, A. M. El-Aziz, R. Hoyer and D. M. Kolb, *Angew. Chem., Int. Ed.*, 2005, **44**, 2080–2084.
- 65 B. Hammer and J. K. Nørskov, *Surf. Sci.*, 1995, **343**, 211–220.
- 66 A. Ruban, B. Hammer, P. Stoltze, H. L. Skriver and J. K. Nørskov, *J. Mol. Catal. A: Chem.*, 1997, **115**, 421–429.
- 67 D. Loffreda, D. Simon and P. Sautet, *Surf. Sci.*, 1999, **425**, 68–80.
- 68 G. X. Wen, Q. Wang, R. G. Zhang, D. B. Li and B. J. Wang, *Phys. Chem. Chem. Phys.*, 2016, **18**, 27272–27283.
- 69 P. Liu, A. Logadottir and J. K. Nørskov, *Electrochim. Acta*, 2003, **48**, 3731–3742.
- 70 P. Liu and J. A. Rodriguez, *J. Chem. Phys.*, 2007, **126**, 164705.
- 71 P. Liu and J. A. Rodriguez, *J. Phys. Chem. B*, 2006, **110**, 19418–19425.
- 72 L. X. Ling, Z. B. Zhao, X. Feng, Q. Wang, B. J. Wang, R. G. Zhang and D. B. Li, *J. Phys. Chem. C*, 2017, **121**, 16399–16414.
- 73 Y. M. Choi and P. Liu, *J. Am. Chem. Soc.*, 2009, **131**, 13054–13061.
- 74 Z. J. Zuo, F. Peng and W. Huang, *Sci. Rep.*, 2016, **6**, 34670.
- 75 X. C. Fu, W. X. Shen, W. Y. Yao and W. H. Hou, *Physical Chemistry*, Higher Education Press, Beijing, 5th edn, 2009, vol. 2, p. 235.
- 76 L. F. Huang, M. Y. Ni, X. H. Zheng, W. H. Zhou, Y. G. Li and Z. Zeng, *J. Phys. Chem. C*, 2010, **114**, 22636–22643.
- 77 X. M. Cao, R. Burch, C. Hardacre and P. Hu, *Catal. Today*, 2011, **165**, 71–79.
- 78 X. C. Fu, W. X. Shen, W. Y. Yao and W. H. Hou, *Physical Chemistry*, Higher Education Press, Beijing, 5th edn, 2009, vol. 2, p. 160.
- 79 M. Mavrikakis, B. Hammer and J. K. Nørskov, *Phys. Rev. Lett.*, 1998, **81**, 2819–2822.
- 80 J. R. Kitchin, J. K. Nørskov, M. A. Barteau and J. G. Chen, *Phys. Rev. Lett.*, 2004, **93**, 156801.
- 81 T. A. Maark and A. A. Peterson, *J. Phys. Chem. C*, 2014, **118**, 4275–4281.
- 82 F. He, K. Li, G. U. Xie, Y. Wang, M. G. Jiao, H. Tang and Z. J. Wu, *J. Power Sources*, 2016, **316**, 8–16.
- 83 J. Cho, S. Lee, S. P. Yoon, J. Han, S. W. Nam, K. Y. Lee and H. C. Ham, *ACS Catal.*, 2017, **7**, 2553–2562.